

3-D Electromagnetic Scattering and Inverse Scattering by Magnetodielectric Objects With Arbitrary Anisotropy in Layered Uniaxial Media

Jiawen Li, Jianliang Zuo^{ID}, Zhen Guan, Feng Han^{ID}, *Member, IEEE*, and Qing Huo Liu^{ID}, *Fellow, IEEE*

Abstract—3-D electromagnetic (EM) scattering and inverse scattering of magnetodielectric objects with arbitrary anisotropy embedded in layered uniaxial media are studied. The stabilized biconjugate gradient fast Fourier transform (BCGS-FFT) method is employed to solve the forward scattering problem formulated by the combined field volume integral equation (CFVIE). In the inversion, we use the variational Born iterative method (VBIM) enhanced by the structural consistency constraint (SCC) to reconstruct eighteen unknown dielectric parameters of the scatterers simultaneously. In order to further improve the accuracy of the reconstructed permittivity, permeability, and conductivity of the scatterers, we propose the structural continuity scanning (SCS) technique. Comparisons between the BCGS-FFT solution and simulated results from finite element method (FEM) are performed to verify the reliability and accuracy of the forward solver. Meanwhile, we reconstruct the multiple anisotropic parameters of several typical structures embedded in layered uniaxial media to show the feasibility and anti-noise ability of the inversion algorithm.

Index Terms—Arbitrary anisotropy, combined field volume integral equation (CFVIE), magnetodielectric, stabilized biconjugate gradient (BCGS), structural consistency constraint (SCC), variational Born iterative method (VBIM).

I. INTRODUCTION

IN THE past three decades, electromagnetic (EM) scattering and inverse scattering have been intensively studied due to their wide applications in microwave imaging [1]–[4], geophysical remote sensing [5], [6], circuit design [7], etc. In sophisticated numerical models, the layered structures and anisotropy of the media [8]–[10] are considered. They have been used to compute the scattered EM fields from

Manuscript received February 14, 2019; revised August 19, 2019; accepted September 1, 2019. Date of publication September 16, 2019; date of current version February 3, 2020. This work was supported by the National Natural Science Foundation of China under Grant 41504120. (*Corresponding author: Feng Han*)

J. Li, J. Zuo, and F. Han are with the Fujian Provincial Key Laboratory of Electromagnetic Wave Science and Detection Technology, Xiamen University, Xiamen 361005, China, and also with the Institute of Electromagnetics and Acoustics, Xiamen University, Xiamen 361005, China (e-mail: feng.han@xmu.edu.cn).

Z. Guan is with the School of Mathematical Sciences, Xiamen University, Xiamen 361005, China.

Q. H. Liu is with the Department of Electrical and Computer Engineering, Duke University, Durham, NC 27708 USA (e-mail: qhliu@duke.edu).

Color versions of one or more of the figures in this article are available online at <http://ieeexplore.ieee.org>.

Digital Object Identifier 10.1109/TAP.2019.2940498

underground reservoirs [11] and composite laminates [12], reconstruct the buried anisotropic objects [13], and design anisotropic microwave devices [14]. Therefore, it is important to study the EM scattering and inverse scattering of arbitrary anisotropic objects embedded in layered media.

In the forward EM scattering modeling, typical numerical methods mainly include integral equation (IE) method, finite difference time domain (FDTD) and finite element method (FEM). The IE method has the intrinsic advantage that only the computation domain enclosing the scatterers needs to be discretized. Green's functions are utilized to account for the EM wave propagation between transmitters as well as receivers and the computation domain. The IE mainly includes volume IE (VIE) [15]–[17], surface IE (SIE) [18], and hybrid volume-SIE (VSIE) [19]. For conductive scatterers, the SIE is preferred. But VIE method is better for dealing with scattering problems of complex inhomogeneous structures. The method of moments (MoM) is the traditional method used to solve VIEs [20]–[23]. However, it has a high computation cost [24].

Researchers have proposed several fast forward scattering algorithms. The first kind is based on subscatterer division, field translation, and redistribution, such as the fast multipole method (FMM) [25] or multilevel fast multipole algorithm (MLFMA) [19]. The second kind is to use the fast Fourier transform (FFT) to accelerate the multiplication of matrices and vectors, such as conjugate gradient FFT (CG-FFT), sparse matrix canonical grid (SMCG) [26], adaptive integration method (AIM) [27], precorrected FFT (pFFT) [28], and stabilized biconjugate gradient FFT (BCGS-FFT) method [24]. BCGS-FFT method uses the hexahedron mesh in the discretization of VIE to facilitate the direct application of FFT acceleration. In addition, BCGS-FFT can be easily combined with inversion algorithms to reconstruct the unknown scatterers which also will be carried out in this article. Therefore, BCGS-FFT is adopted in our forward scattering model.

The methods for solving inverse scattering problems can be roughly divided into two categories. One is the linear inversion method, such as Born approximation or regularization method [29]–[31]. The other is to transform the nonlinear inverse scattering problem into an optimization problem, and then solve it iteratively [2], [32], [33]. The linear inversion method has fast convergence speed and does not need to solve the

gradient of scattered fields. However, because the multiple scattering of the objects is not taken into account, it can only invert for objects with small electrical sizes or low contrasts. The nonlinear inversion methods can deal with multiple scattering and high contrast objects. But nonlinearity and ill-posedness can cause the iterative convergence unstable and slow. Researchers have proposed several methods to solve the nonlinear scattering problem, such as Born iterative method (BIM) [2], [34], distorted BIM (DBIM) [32], [35], subspace-based DBIM [36], variational BIM (VBIM) [5], [37], contrast source inversion (CSI) method [33], [38] as well as subspace-based optimization method (SOM) [39]–[43]. VBIM converges faster than BIM and consumes less memory than DBIM. It has been combined with the structural consistency constraint (SCC) to invert for the biaxial anisotropic scatterers in our previous work [13].

In this article, we use the BCGS-FFT and VBIM to solve the scattering and inverse scattering problems of magnetodielectric objects with arbitrary anisotropy embedded in layered uniaxial media. Although several related works have been accomplished previously, our research has the following new contributions.

- 1) The contrast of anisotropic permeability is considered while previous works [8], [41], [44] only included the dielectric contrasts. Therefore, combined field VIE (CFVIE) is used [45].
- 2) A structural continuity scanning (SCS) algorithm is proposed to further improve reconstructed results by VBIM-SCC which is proposed in [13].
- 3) For the first time, 18 parameters of the symmetrical permittivity, permeability as well as conductivity tensors for arbitrary anisotropic scatterers are retrieved simultaneously.

One should note that the anisotropy tensors are assumed symmetrical in this article, which is common for natural and man-made materials [46].

The organization of this article is as follows. In Section II, the mathematical formulation of the CFVIE for EM forward scattering of 3-D arbitrary anisotropic objects embedded in layered uniaxial media is derived, and weak forms of the CFVIE are given. Meanwhile, the inversion model is discussed, and the SCS algorithm used to enhance the VBIM-SCC results is presented. In Section III, we verify the forward computation results by comparing them with the numerical simulations of FEM by the commercial software COMSOL. In Section IV, several typical anisotropic scatterers are reconstructed. Accuracy improvement by SCS is shown, and the anti-noise ability of the inversion algorithm is verified. Finally, in Section V, conclusions are drawn and discussions are presented.

II. FORMULATION

The objective of this article is to solve the scattering and inverse scattering problems of inhomogeneous 3-D magnetodielectric objects with arbitrary anisotropy embedded in layered uniaxial media. The typical configuration of scattering and inverse scattering is shown in Fig. 1. We assume the object

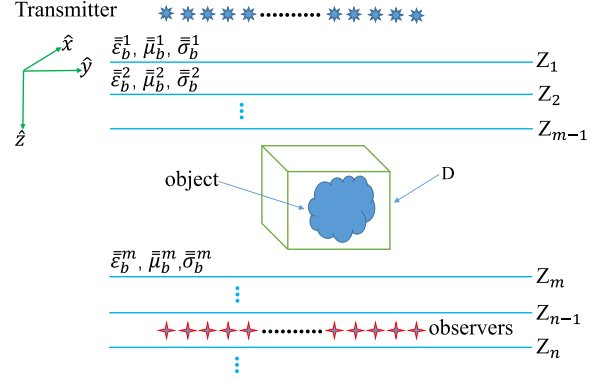


Fig. 1. Typical configuration for EM scattering in a planarly layered uniaxial anisotropic medium.

is completely embedded in the m th layer, and has arbitrary anisotropy for permittivity, permeability, and conductivity. The relative parameter tensors of the i th layer are written as

$$\bar{\xi}_b^i = \begin{bmatrix} \zeta_{11}^b & \zeta_{12}^b & \zeta_{13}^b \\ \zeta_{21}^b & \zeta_{22}^b & \zeta_{23}^b \\ \zeta_{31}^b & \zeta_{32}^b & \zeta_{33}^b \end{bmatrix} = \text{diag}\{\zeta_{11}^b, \zeta_{22}^b, \zeta_{33}^b\} \quad (1)$$

where ζ can be ϵ , σ or μ , $\zeta_{11}^b = \zeta_{22}^b$, and the subscript and superscript b means the background. For convenience, the relative complex permittivity of the i th layer is written as

$$\bar{\epsilon}_b^i = \bar{\epsilon}_b^i + \frac{\bar{\sigma}_b^i}{j\omega\epsilon_0} \quad (2)$$

where ω is the angular frequency of the EM wave. The relative permittivity, permeability, and conductivity tensors of the scatterer with arbitrary anisotropy are written as

$$\bar{\xi}_s = \begin{bmatrix} \zeta_s & \zeta_{12}^s & \zeta_{13}^s \\ \zeta_{21}^s & \zeta_s & \zeta_{23}^s \\ \zeta_{31}^s & \zeta_{32}^s & \zeta_s \end{bmatrix} \quad (3)$$

where s denotes the scatterer, and $\zeta_{pq}^s = \zeta_{qp}^s$ with $p, q = 1, 2$ and 3 . Similarly, the complex relative permittivity tensor of the scatterer can be written as

$$\bar{\epsilon}_s = \bar{\epsilon}_s + \frac{\bar{\sigma}_s}{j\omega\epsilon_0}. \quad (4)$$

A. Forward Model

According to the volume equivalence principle [47], the scattered electric fields \mathbf{E}_{sct} and \mathbf{H}_{sct} are equal to the fields radiated by the equivalent electric current source \mathbf{J}_{eq} and equivalent magnetic current source \mathbf{M}_{eq} inside the arbitrary anisotropic objects which can be expressed as

$$\mathbf{J}_{eq}(\mathbf{r}) = j\omega\bar{\chi}_\epsilon(\mathbf{r})\mathbf{D}_{tot}(\mathbf{r}) \quad (5a)$$

$$\mathbf{M}_{eq}(\mathbf{r}) = j\omega\bar{\chi}_\mu(\mathbf{r})\mathbf{B}_{tot}(\mathbf{r}) \quad (5b)$$

where the tensors

$$\bar{\chi}_\epsilon(\mathbf{r}) = [\bar{\epsilon}(\mathbf{r}) - \bar{\epsilon}_b]\bar{\epsilon}^{-1}(\mathbf{r}) \quad (6a)$$

$$\bar{\chi}_\mu(\mathbf{r}) = [\bar{\epsilon}(\mathbf{r}) - \bar{\epsilon}_b]\bar{\epsilon}^{-1}(\mathbf{r}) \quad (6b)$$

are the dielectric and magnetic contrast functions. $\bar{\epsilon}(\mathbf{r})$ and $\bar{\mu}(\mathbf{r})$ are the relative complex permittivity tensor and relative permeability tensor at any point \mathbf{r} in the whole space. $\mathbf{D}_{tot} = \bar{\epsilon}\epsilon_0\mathbf{E}_{tot}$ and $\mathbf{B}_{tot} = \bar{\mu}\mu_0\mathbf{H}_{tot}$ are the total electric flux density and magnetic flux density, respectively. The scattered electric and magnetic fields can be computed by

$$\begin{aligned}\mathbf{E}_{sct}^n(\mathbf{r}) &= j\omega \int_D \bar{\mathbf{G}}_{\mathbf{EJ}}^{nm}(\mathbf{r}, \mathbf{r}') \cdot \bar{\chi}_\epsilon(\mathbf{r}') \mathbf{D}_{tot}^m(\mathbf{r}') d\mathbf{r}' \\ &\quad + j\omega \int_D \bar{\mathbf{G}}_{\mathbf{EM}}^{nm}(\mathbf{r}, \mathbf{r}') \cdot \bar{\chi}_\mu(\mathbf{r}') \mathbf{B}_{tot}^m(\mathbf{r}') d\mathbf{r}'\end{aligned}\quad (7a)$$

$$\begin{aligned}\mathbf{H}_{sct}^n(\mathbf{r}) &= j\omega \int_D \bar{\mathbf{G}}_{\mathbf{HJ}}^{nm}(\mathbf{r}, \mathbf{r}') \cdot \bar{\chi}_\epsilon(\mathbf{r}') \mathbf{D}_{tot}^m(\mathbf{r}') d\mathbf{r}' \\ &\quad + j\omega \int_D \bar{\mathbf{G}}_{\mathbf{HM}}^{nm}(\mathbf{r}, \mathbf{r}') \cdot \bar{\chi}_\mu(\mathbf{r}') \mathbf{B}_{tot}^m(\mathbf{r}') d\mathbf{r}'\end{aligned}\quad (7b)$$

where $\bar{\mathbf{G}}_{\mathbf{EJ}}^{nm}$, $\bar{\mathbf{G}}_{\mathbf{EM}}^{nm}$, $\bar{\mathbf{G}}_{\mathbf{HJ}}^{nm}$, and $\bar{\mathbf{G}}_{\mathbf{HM}}^{nm}$ are the layered dyadic Green's functions (DGFs) [48] connecting the equivalent electric current source and equivalent magnetic current source in the m th layer and the receiver in the n th layer, and D is the computation domain enclosing the scatterers and located in the m th layer. It is easy to formulate the CFVIE as

$$\begin{aligned}\mathbf{E}_{inc}^n(\mathbf{r}) &= \mathbf{E}_{tot}^n(\mathbf{r}) - \mathbf{E}_{sct}^n(\mathbf{r}) = \bar{\epsilon}^{-1}(\mathbf{r}) \frac{\mathbf{D}_{tot}^n(\mathbf{r})}{\epsilon_0} \\ &\quad - j\omega \int_D \bar{\mathbf{G}}_{\mathbf{EJ}}^{nm}(\mathbf{r}, \mathbf{r}') \cdot \bar{\chi}_\epsilon(\mathbf{r}') \mathbf{D}_{tot}^m(\mathbf{r}') d\mathbf{r}' \\ &\quad - j\omega \int_D \bar{\mathbf{G}}_{\mathbf{EM}}^{nm}(\mathbf{r}, \mathbf{r}') \cdot \bar{\chi}_\mu(\mathbf{r}') \mathbf{B}_{tot}^m(\mathbf{r}') d\mathbf{r}'\end{aligned}\quad (8a)$$

$$\begin{aligned}\mathbf{H}_{inc}^n(\mathbf{r}) &= \mathbf{H}_{tot}^n(\mathbf{r}) - \mathbf{H}_{sct}^n(\mathbf{r}) = \bar{\mu}^{-1}(\mathbf{r}) \frac{\mathbf{B}_{tot}^n(\mathbf{r})}{\mu_0} \\ &\quad - j\omega \int_D \bar{\mathbf{G}}_{\mathbf{HJ}}^{nm}(\mathbf{r}, \mathbf{r}') \cdot \bar{\chi}_\epsilon(\mathbf{r}') \mathbf{D}_{tot}^m(\mathbf{r}') d\mathbf{r}' \\ &\quad - j\omega \int_D \bar{\mathbf{G}}_{\mathbf{HM}}^{nm}(\mathbf{r}, \mathbf{r}') \cdot \bar{\chi}_\mu(\mathbf{r}') \mathbf{B}_{tot}^m(\mathbf{r}') d\mathbf{r}'\end{aligned}\quad (8b)$$

where \mathbf{E}_{inc}^n and \mathbf{H}_{inc}^n are the incident fields evaluated in the n th layer when the scatterers are absent. The flux \mathbf{D}_{tot} and \mathbf{B}_{tot} are used to replace \mathbf{E}_{tot} and \mathbf{H}_{tot} because the divergence conforming basis function will be adopted. Once the total flux \mathbf{D}_{tot} and \mathbf{B}_{tot} in the n th layer are acquired, the scattered fields anywhere can be obtained through (7).

Before solving the CFVIE (8), we discretize them first to obtain the linear systems. In this article, we use the same rooftop basis and testing functions, and take the similar procedure as in [8]. The flux densities are expanded by the 3-D volumetric roof-top basis function

$$D_{tot}^{n(q)}(\mathbf{r}) = \epsilon_0 \sum_{\mathbf{i}} d_{\mathbf{i}}^{(q)} \psi_{\mathbf{i}}^{(q)}(\mathbf{r}) \quad (9a)$$

$$B_{tot}^{n(q)}(\mathbf{r}) = \mu_0 \sum_{\mathbf{i}} b_{\mathbf{i}}^{(q)} \psi_{\mathbf{i}}^{(q)}(\mathbf{r}) \quad (9b)$$

where $q = 1, 2, 3$ are corresponding to \hat{x} , \hat{y} , and \hat{z} three components, respectively, and $\mathbf{i} = \{I, J, K\}$ are the indexes of the discretized cells for three components, respectively. $d_{\mathbf{i}}^{(q)}$ and $b_{\mathbf{i}}^{(q)}$ are the expansion coefficients for $D^{(q)}$ and $B^{(q)}$, respectively, and $\psi^{(q)}$ is the basis function with the detailed

expression given in [49]. The incident fields are expanded in a similar way

$$E_{inc}^{n(q)}(\mathbf{r}) = \sum_{\mathbf{i}} E_{\mathbf{i}}^{i,(q)} \psi_{\mathbf{i}}^{(q)}(\mathbf{r}) \quad (10a)$$

$$H_{inc}^{n(q)}(\mathbf{r}) = \sum_{\mathbf{i}} H_{\mathbf{i}}^{i,(q)} \psi_{\mathbf{i}}^{(q)}(\mathbf{r}). \quad (10b)$$

After testing both sides of the CFVIE (8) with the same rooftop function $\psi_{\mathbf{m}}^{(p)}(\mathbf{r})$ with $p = 1, 2, 3$ for three orthogonal directions, and $\mathbf{m} = \{M, N, P\}$ the indexes of the discretized cells, we obtain the domain-integral weak forms of the CFVIE

$$e_{\mathbf{m}}^{i,(p)} = \sum_{\mathbf{i}} \sum_{q=1}^3 d_{\mathbf{i}}^{(q)} u_{\mathbf{m};\mathbf{i}}^{e,(p,q)} - E_{\mathbf{i}}^{s,(q)} v_{\mathbf{m};\mathbf{i}}^{(p,q)} \quad (11a)$$

$$h_{\mathbf{m}}^{i,(p)} = \sum_{\mathbf{i}} \sum_{q=1}^3 b_{\mathbf{i}}^{(q)} u_{\mathbf{m};\mathbf{i}}^{h,(p,q)} - H_{\mathbf{i}}^{s,(q)} v_{\mathbf{m};\mathbf{i}}^{(p,q)} \quad (11b)$$

where

$$u_{\mathbf{m};\mathbf{i}}^{e,(p,q)} = \int_D \psi_{\mathbf{m}}^{(p)}(\mathbf{r}) \bar{\epsilon}^{-1}(\mathbf{r}) \psi_{\mathbf{i}}^{(q)}(\mathbf{r}) d\mathbf{r} \quad (12a)$$

$$u_{\mathbf{m};\mathbf{i}}^{h,(p,q)} = \int_D \psi_{\mathbf{m}}^{(p)}(\mathbf{r}) \bar{\mu}^{-1}(\mathbf{r}) \psi_{\mathbf{i}}^{(q)}(\mathbf{r}) d\mathbf{r} \quad (12b)$$

and $e_{\mathbf{m}}^{i,(p)}$, $h_{\mathbf{m}}^{i,(p)}$, and $v_{\mathbf{m};\mathbf{i}}^{(p,q)}$ are referred to [49]. $E_{\mathbf{i}}^{s,(q)}$ and $H_{\mathbf{i}}^{s,(q)}$ are components of the scattered fields $\mathbf{E}_{\mathbf{i}}^s$ and $\mathbf{H}_{\mathbf{i}}^s$ respectively which are computed by

$$\begin{aligned}\mathbf{E}_{\mathbf{i}}^s &= j\omega \Delta V \cdot \left(\epsilon_0 \sum_{\mathbf{i}'} \bar{\mathbf{G}}_{\mathbf{EJ}}^{nm}(\mathbf{i}, \mathbf{i}') \cdot (\bar{\chi}_{\epsilon, \mathbf{i}'} \cdot \mathbf{d}_{\mathbf{i}'}) \right. \\ &\quad \left. + \mu_0 \sum_{\mathbf{i}'} \bar{\mathbf{G}}_{\mathbf{EM}}^{nm}(\mathbf{i}, \mathbf{i}') \cdot (\bar{\chi}_{\mu, \mathbf{i}'} \cdot \mathbf{b}_{\mathbf{i}'}) \right)\end{aligned}\quad (13a)$$

$$\begin{aligned}\mathbf{H}_{\mathbf{i}}^s &= j\omega \Delta V \cdot \left(\epsilon_0 \sum_{\mathbf{i}'} \bar{\mathbf{G}}_{\mathbf{HJ}}^{nm}(\mathbf{i}, \mathbf{i}') \cdot (\bar{\chi}_{\epsilon, \mathbf{i}'} \cdot \mathbf{d}_{\mathbf{i}'}) \right. \\ &\quad \left. + \mu_0 \sum_{\mathbf{i}'} \bar{\mathbf{G}}_{\mathbf{HM}}^{nm}(\mathbf{i}, \mathbf{i}') \cdot (\bar{\chi}_{\mu, \mathbf{i}'} \cdot \mathbf{b}_{\mathbf{i}'}) \right)\end{aligned}\quad (13b)$$

where $\mathbf{i} = \{I, J, K\}$ are indexes for field point cells while $\mathbf{i}' = \{I', J', K'\}$ are indexes for equivalent current cells. $\Delta V = \Delta x \Delta y \Delta z$ is the discretized cell volume. $\mathbf{d}_{\mathbf{i}'}$ is a vector containing $d_{I', J', K'}^{(q)}$ and $\mathbf{b}_{\mathbf{i}'}$ is a vector containing $b_{I', J', K'}^{(q)}$ with $q = 1, 2, 3$. By performing the integrals in $u_{\mathbf{m};\mathbf{i}}^{e,(p,q)}$, $u_{\mathbf{m};\mathbf{i}}^{h,(p,q)}$, and $v_{\mathbf{m};\mathbf{i}}^{(p,q)}$, we obtain the complete weak forms

$$\begin{aligned}e_{\mathbf{m}}^{i,(p)} &= \sum_{q=p}^{p+2} \sum_{l=1}^3 \mathbf{S}_{\mathbf{m},l}^{e,(q)} [d_{\mathbf{m}+\hat{x}_p(l-2)}^{(q)} + (1 - \delta_{p,q}) d_{\mathbf{m}+\hat{x}_p(l-2)+\hat{x}_q}^{(q)}] \\ &\quad - \sum_{l=1}^3 \mathbf{Q}_{\mathbf{m},l} E_{\mathbf{m}+\hat{x}_p(l-2)}^{s,(p)}\end{aligned}\quad (14a)$$

$$\begin{aligned}h_{\mathbf{m}}^{i,(p)} &= \sum_{q=p}^{p+2} \sum_{l=1}^3 \mathbf{S}_{\mathbf{m},l}^{\mu,(q)} [b_{\mathbf{m}+\hat{x}_p(l-2)}^{(q)} + (1 - \delta_{p,q}) b_{\mathbf{m}+\hat{x}_p(l-2)+\hat{x}_q}^{(q)}] \\ &\quad - \sum_{l=1}^3 \mathbf{Q}_{\mathbf{m},l} H_{\mathbf{m}+\hat{x}_p(l-2)}^{s,(p)}\end{aligned}\quad (14b)$$

where $p, q, p+1, q+1, p+2, q+2$ are cyclic indexes with the period of 3, and $\delta_{p,q}$ is the Kronecker symbol. \hat{x}_p is the unit vector in the p th direction. $\mathbf{S}_{\mathbf{m},l}^{\varepsilon,(q)}$ is the l th component of the vector $\mathbf{S}_{\mathbf{m}}^{\varepsilon,(q)}$ whose expression is given in [8]. $\mathbf{Q}_{\mathbf{m}}$ is a column vector and written as $(\Delta V/6)[1 \ 4 \ 1]^T$ where T is the matrix transpose. $\mathbf{S}_{\mathbf{m},l}^{\mu,(q)}$ can be derived from $\mathbf{S}_{\mathbf{m},l}^{\varepsilon,(q)}$ by replacing ε with μ . In the discretized CFVIE (14), the coefficient d^q and b^q are the unknowns to be solved. The BCGS fast solver is employed to solve them iteratively. As shown in (13), the interactions between DGFs and discretized equivalent current are convolutions in the horizontal plane and can be decomposed into convolution and correlation in the z direction, which has been discussed in our previous article [8]. Therefore, FFT is used to accelerate the computation of (13) in each BCGS iteration step. This lowers the computation time complexity from $O(KM^2)$ to $O(KM\log M)$ where K is the iteration number and M is the number of unknowns in the discretized computation domain.

B. Inversion Model

In the inversion model, the scattered fields \mathbf{E}_{sct} and \mathbf{H}_{sct} can be measured and tensors $\bar{\varepsilon}_s$, $\bar{\mu}_s$ and $\bar{\sigma}_s$ are the unknowns. We assume M_T sources, M_R receivers, and M_F operation frequencies are used to collect the scattered fields. The rectangular reconstructed region is divided into $N = N_1 \times N_2 \times N_3$ small cells, and each cell has 18 unknowns to be solved for the arbitrary anisotropic objects. The discretized data equation for the i th frequency can be written as

$$\mathbf{L}(\omega_i) = \mathbf{A}(\omega_i)\mathbf{x}(\omega_i) \quad (15)$$

where ω_i is the i th angular frequency. $\mathbf{L}(\omega_i)$ is a $6M_T M_R$ column vector containing the measured scattered data whose column elements are expressed as

$$\mathbf{L}(\omega_i) = \begin{bmatrix} \mathbf{E}_{sct}(\mathbf{r}_{iR}, \mathbf{r}_{iT}, \omega_i) \\ \eta_0 \mathbf{H}_{sct}(\mathbf{r}_{iR}, \mathbf{r}_{iT}, \omega_i) \end{bmatrix} \quad (16)$$

The η_0 is the intrinsic impedance of air. And $\mathbf{A}(\omega_i)\mathbf{x}(\omega_i)$ represents the reconstructed scattered fields. $\mathbf{A}(\omega_i)$ is a $6M_T M_R \times 12N$ matrix, whose elements for the k th cell are

$$\mathbf{A}(\omega_i) = \Delta V \begin{bmatrix} \mathbf{A}_1(\omega_i) & \mathbf{A}_2(\omega_i) \\ \eta_0 \mathbf{A}_3(\omega_i) & \eta_0 \mathbf{A}_4(\omega_i) \end{bmatrix} \quad (17)$$

where

$$\mathbf{A}_1(\omega_i) = j\omega_i \epsilon_0 \overline{\overline{\mathbf{G}}}_{\mathbf{EJ}}^{\text{nm}}(\mathbf{r}_{iR}, \mathbf{r}'_k, \omega_i) \mathbf{E}_{tot}(\mathbf{r}'_k, \mathbf{r}_{iT}, \omega_i) \quad (18a)$$

$$\mathbf{A}_2(\omega_i) = j\omega_i \mu_0 \overline{\overline{\mathbf{G}}}_{\mathbf{EM}}^{\text{nm}}(\mathbf{r}_{iR}, \mathbf{r}'_k, \omega_i) \mathbf{H}_{tot}(\mathbf{r}'_k, \mathbf{r}_{iT}, \omega_i) \quad (18b)$$

$$\mathbf{A}_3(\omega_i) = j\omega_i \epsilon_0 \overline{\overline{\mathbf{G}}}_{\mathbf{HJ}}^{\text{nm}}(\mathbf{r}_{iR}, \mathbf{r}'_k, \omega_i) \mathbf{E}_{tot}(\mathbf{r}'_k, \mathbf{r}_{iT}, \omega_i) \quad (18c)$$

$$\mathbf{A}_4(\omega_i) = j\omega_i \mu_0 \overline{\overline{\mathbf{G}}}_{\mathbf{HM}}^{\text{nm}}(\mathbf{r}_{iR}, \mathbf{r}'_k, \omega_i) \mathbf{H}_{tot}(\mathbf{r}'_k, \mathbf{r}_{iT}, \omega_i) \quad (18d)$$

$\mathbf{x}(\omega_i)$ is the unknown to be solved for arbitrary anisotropic objects, whose elements for each cell can be written as $[\mathbf{x}_1(\omega_i) \ \mathbf{x}_2]^T$. $\mathbf{x}_1(\omega_i)$ is a complex row vector having six elements. Each element is $(\varepsilon_{pq}^s - \varepsilon_{pq}^b) + (1/j\omega_i \epsilon_0)(\sigma_{pq}^s - \sigma_{pq}^b)$ with $p, q = 1, 2, 3$ and $p \leq q$. Similarly, \mathbf{x}_2 is also a six elements row vector and each of them is $\mu_{pq}^s - \mu_{pq}^b$. Obviously, the unknown \mathbf{x} is different for different operation frequencies.

Therefore, the data equation (15) is reformulated as the real equation with the same unknown for all operation frequencies, whose expression is rewritten as

$$\mathbf{L}' = \mathbf{A}' \mathbf{y} \quad (19)$$

where \mathbf{L}' is the combination of the real parts and imaginary parts of the measured scattered fields for all operation frequencies. The total number of elements in \mathbf{L}' is $M = 12M_T M_R M_F$. They are evaluated by

$$\mathbf{L}'(\omega_i) = \begin{bmatrix} \text{Re}(\mathbf{E}_{sct}(\mathbf{r}_{iR}, \mathbf{r}_{iT}, \omega_i)) \\ \text{Re}(\eta_0 \mathbf{H}_{sct}(\mathbf{r}_{iR}, \mathbf{r}_{iT}, \omega_i)) \\ \text{Im}(\mathbf{E}_{sct}(\mathbf{r}_{iR}, \mathbf{r}_{iT}, \omega_i)) \\ \text{Im}(\eta_0 \mathbf{H}_{sct}(\mathbf{r}_{iR}, \mathbf{r}_{iT}, \omega_i)) \end{bmatrix} \quad (20)$$

for the i th frequency. \mathbf{A}' is a $M \times 18N$ matrix, whose elements for each frequency are

$$\begin{aligned} \mathbf{A}'(\omega_i) &= \Delta V \begin{bmatrix} \text{Re}(\mathbf{A}_1(\omega_i)) & \text{Im}\left(\frac{\mathbf{A}_1(\omega_i)}{\omega_i \epsilon_0}\right) & \text{Re}(\mathbf{A}_2(\omega_i)) \\ \eta_0 \text{Re}(\mathbf{A}_3(\omega_i)) & \eta_0 \text{Im}\left(\frac{\mathbf{A}_3(\omega_i)}{\omega_i \epsilon_0}\right) & \eta_0 \text{Re}(\mathbf{A}_4(\omega_i)) \\ \text{Im}(\mathbf{A}_1(\omega_i)) & \text{Re}\left(-\frac{\mathbf{A}_1(\omega_i)}{\omega_i \epsilon_0}\right) & \text{Im}(\mathbf{A}_2(\omega_i)) \\ \eta_0 \text{Im}(\mathbf{A}_3(\omega_i)) & \eta_0 \text{Re}\left(-\frac{\mathbf{A}_3(\omega_i)}{\omega_i \epsilon_0}\right) & \eta_0 \text{Im}(\mathbf{A}_4(\omega_i)) \end{bmatrix}. \end{aligned} \quad (21)$$

The column vector \mathbf{y} has $18N$ real unknowns. For each cell, it can be written as $[\mathbf{y}_1 \ \mathbf{y}_2 \ \mathbf{y}_3]^T$. The \mathbf{y}_1 is a row vector having six elements. Each of them is $\varepsilon_{pq}^s - \varepsilon_{pq}^b$ with $p, q = 1, 2, 3$ and $p \leq q$. Similarly, \mathbf{y}_2 and \mathbf{y}_3 are also six elements row vectors which are constructed for the anisotropic conductivity and permeability, respectively.

In order to solve the data equation (19) by VBIM, we normalize the elements of \mathbf{y} by parameters of the background medium to keep them the same order of magnitude. Therefore, the normalized \mathbf{y} is the contrast and denoted as \mathbf{y}' . The matrix \mathbf{A}' is modified accordingly and denoted as \mathbf{B} to keep the data equation (19) correct. By taking the variation of the data equation (19) with respect to \mathbf{y}' , we obtain

$$\delta \mathbf{L}'_n = \mathbf{B}_n \delta \mathbf{y}'_{n+1} \quad (22)$$

where $\delta \mathbf{L}'_n$ is the difference between the measured data and the reconstructed data in the n th iteration. \mathbf{B}_n can be acquired from (18) and (21). As the initial value of unknown \mathbf{y}' , \mathbf{y}'_1 is set as zero. And $\delta \mathbf{y}'_{n+1}$ of the $(n+1)$ th iteration is defined as

$$\delta \mathbf{y}'_{n+1} = \mathbf{y}'_{n+1} - \mathbf{y}'_n. \quad (23)$$

The cost function with the regularization term in the $(n+1)$ th iteration step is defined as

$$F(\delta \mathbf{y}'_{n+1}) = \frac{\|\delta \mathbf{L}'_n - \mathbf{B}_n \delta \mathbf{y}'_{n+1}\|^2}{\|\delta \mathbf{L}'_n\|^2} + \gamma^2 \frac{\|\delta \mathbf{y}'_{n+1}\|^2}{\|\delta \mathbf{y}'_n\|^2} \quad (24)$$

where γ is the regularization factor, and $\|\cdot\|$ is the L2 norm. $\|\delta \mathbf{y}'_{n+1}\|^2 / \|\delta \mathbf{y}'_n\|^2$ is a self-adaptive regularization coefficient, which can make the process of inversion more stable [6]. The minimization of the cost function is equivalent to solving the following [50]:

$$\left(\mathbf{B}_n^T \mathbf{B}_n + \gamma^2 \frac{\|\delta \mathbf{L}'_n\|^2}{\|\delta \mathbf{y}'_n\|^2} \mathbf{I} \right) \delta \mathbf{y}'_{n+1} = \mathbf{B}_n^T \delta \mathbf{L}'_n. \quad (25)$$

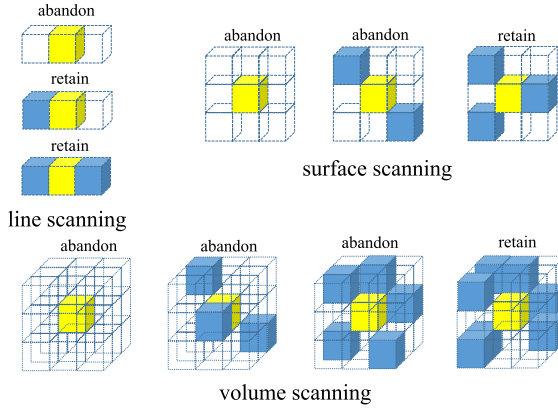


Fig. 2. SCS in three different dimensions. The yellow cell is judged by VBIM-SCC as “scatterer” and will be checked by SCS. The transparent cells are the “background” cells. The blue cells are the adjacent “scatterer” cells.

This equation can be efficiently solved by the CG method [51]. In addition, a nonlinear transform is adopted to constrain the reconstructed parameters in reasonable ranges in the inversion process [34], [52].

C. Structural Consistency Constraint and Structural Continuity Scanning

As discussed in Section II-B, there are totally 18 unknown parameters in each discretized cell for arbitrary anisotropic scatterers. This makes the inversion more challenging than the isotropic inversion problem. On the other hand, 18 unknown parameters share the same geometry structure, which can be treated as the additional constraint in the VBIM inversion. Therefore, the Monte Carlo method is used to obtain the structures of the scatterers, i.e., to judge whether a certain discretized cell in the inversion domain is the “scatterer” or “background.” If it is judged as the “background,” it will be discarded in the next VBIM iteration since it has no contribution to the measured scattered data. In this way, the inversion domain is compressed and the computation cost is lowered. This is the SCC algorithm, and has been successfully applied to the inversion of biaxial scatterers in our previous article [13], and will not be repeated here.

However, SCC is based on Monte Carlo method. Some “background” cells may be incorrectly judged as “scatterer” cells. As a result, some faked isolated tiny “scatterer” blocks will show up in the final reconstructed result, which leads to the deviation of the retrieved parameter values of the true “scatterer” blocks away from their true values. In order to resolve this issue, we propose the SCS algorithm. For a certain discretized cell in the inversion domain, if it is judged as “scatterer,” we track its adjacent cells and check whether they are “scatterer” or “background” cells, as shown in Fig. 2. The SCS is performed in three different dimensions, i.e., the line scanning, surface scanning, and volume scanning. A certain cell which has been judged as “scatterer” by VBIM-SCC will be regarded as faked one if it cannot survive in any scanning. In addition, it should be noted that the line scanning is performed in three orthogonal directions simultaneously, and

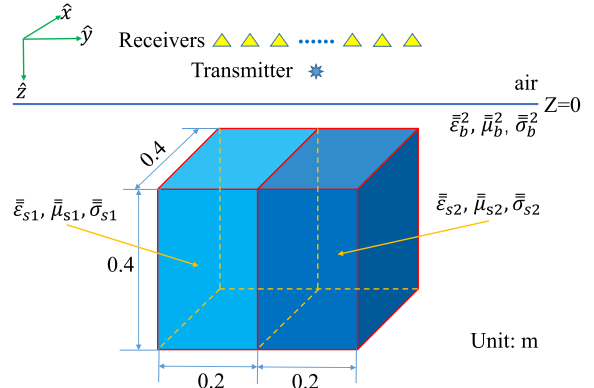


Fig. 3. Configuration of a two-block cubic scatterer with the dimensions of 0.4 m × 0.4 m × 0.4 m embedded in a half-space uniaxial anisotropic background medium.

the surface scanning is performed in three orthogonal planes simultaneously. Let us take the line scanning as an example. As shown in Fig. 2, we count the number of “scatterer” cells connected to a certain cell which has already been judged as “scatterer” by VBIM-SCC and will be checked by SCS. If this number is larger or equal to one, the current cell will be retained, or it will be regarded as faked one and abandoned in the next VBIM iteration. But note the above condition must be satisfied simultaneously in all three directions. For the surface scanning and volume scanning, the SCS is implemented in a similar way. The only difference is the threshold of the number of adjacent “scatterer” cells. They are three for surface scanning and seven for volume scanning. The threshold values for three different scanning schemes are chosen according to the worst case, i.e., assuming the current cell checked by SCS at the vertex of a cube.

III. FORWARD VALIDATION

In this section, we validate the forward BCGS-FFT solver by comparing the results with numerical simulations of FEM by the commercial software COMSOL. The source is a unit electric dipole, operating at 1 GHz and polarized at the direction of (1, 1, 1). Such a source polarization means three components of the dipole moment in the rectangular coordinate system have the same intensity. In order to mimic the EM radiation from antennas, we set the first layer air and put both the transmitter and the receiver arrays in this layer. The stop criterion of the BCGS iteration residual error is set to be 10^{-5} . Fig. 3 shows the forward scattering model for a two-block uniaxial anisotropic cube embedded in a half-space background medium. The two-block cube with the size of 0.4 m × 0.4 m × 0.4 m is located at the bottom layer of the half-space background. The top layer of the background is air, i.e., $\bar{\epsilon}_b^1 = \bar{\mathbf{I}}$, $\bar{\mu}_b^1 = \bar{\mathbf{I}}$ and $\bar{\sigma}_b^1 = 0$. The boundary is at $z = 0$. The bottom layer has the dielectric parameters

$$\bar{\epsilon}_b^2 = \text{diag}\{1.5, 1.5, 2.0\} \quad (26a)$$

$$\bar{\mu}_b^2 = \text{diag}\{1.0, 1.0, 1.5\} \quad (26b)$$

$$\bar{\sigma}_b^2 = \text{diag}\{1, 1, 2\} \text{ mS/m.} \quad (26c)$$

TABLE I
SCATTERER DIELECTRIC PARAMETERS IN THE FORWARD MODEL

Parameter	ε_{11}	ε_{12}	ε_{13}	ε_{22}	ε_{23}	ε_{33}	μ_{11}	μ_{12}	μ_{13}	μ_{22}	μ_{23}	μ_{33}	σ_{11}	σ_{12}	σ_{13}	σ_{22}	σ_{23}	σ_{33}
block																		
left	1.0	0.6	0.4	1.3	0.3	1.5	1.3	0.1	0.4	1.3	0.3	1.2	5	3	3	4	3	5
right	2.4	0.3	0.5	2.0	0.3	1.5	1.4	0.1	0.2	1.4	0.3	1.0	2	3	4	3	3	4

Remark: the unit of σ is mS/m.

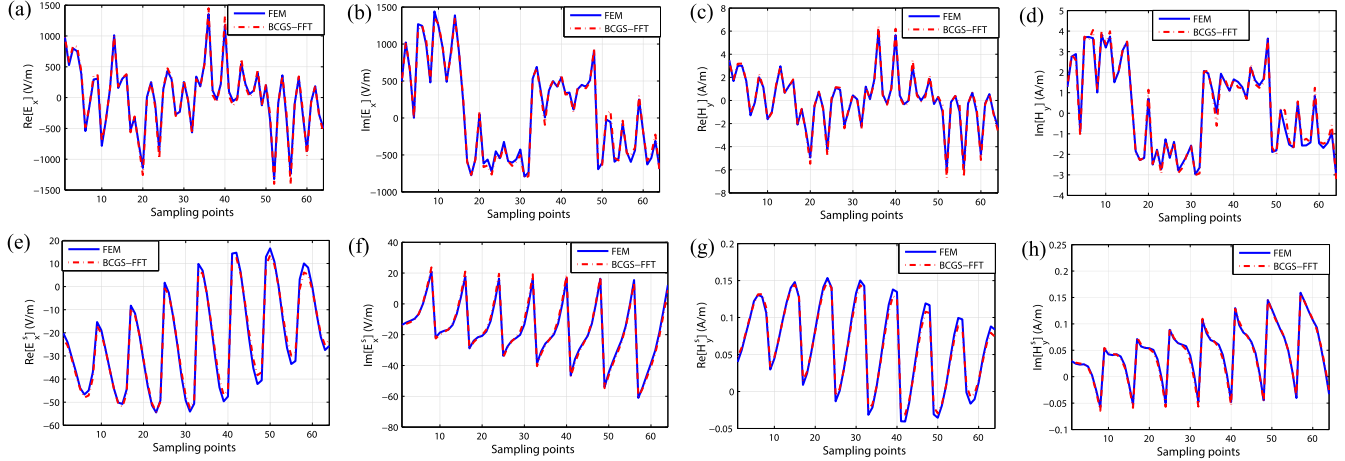


Fig. 4. Comparisons of the total electric and magnetic fields inside the cube and the scattered fields at the receiver array solved by BCGS-FFT and simulated by FEM. (a) Real parts of E_x of total fields. (b) Imaginary parts of E_x of total fields. (c) Real parts of E_x of scattered fields. (d) Imaginary parts of E_x of scattered fields. (e) Real parts of H_y of total fields. (f) Imaginary parts of H_y of total fields. (g) Real parts of H_y of scattered fields. (h) Imaginary parts of H_y of scattered fields.

Two blocks of the scatterer have the same thickness 0.2 m, and their dielectric parameters are listed in Table I. The centers of the left block and right block are at $(-0.1, 0, 0.4)$ m and $(0.1, 0, 0.4)$ m, respectively. The transmitter electric dipole is located at $(0, 0, -0.1)$ m. The computation domain of BCGS-FFT has the same size as that of the scatterer and is discretized into 50^3 cubic cells with 750 thousand unknowns. Thus, the sampling density (SD) is larger than 17 points per wavelength (PPW) inside the cube. For comparisons of total fields, we only pick 64 uniform sampling points inside the scatterer. For scattered field comparisons, we place the receivers at the $z = -0.3$ m plane. The array consists of 64 receivers which uniformly distribute in a 0.175 m \times 0.175 m square area, as shown in Fig. 3.

The BCGS-FFT iteration converges after 48 steps with the residual error of 3.32×10^{-6} . Fig. 4 shows comparisons of the x -components of total electric fields and y -components of total magnetic fields inside the computation domain and scattered fields at the receiver array. We can see the BCGS-FFT solutions match the FEM computation results well. Comparisons of other components have the same good match and are not shown here.

IV. INVERSION ASSESSMENT

In this section, we perform the inversion to reconstruct objects with arbitrary anisotropy embedded in layered uniaxial media. The measured scattered field data are simulated by the BCGS-FFT forward solver validated in Section III. The first two models are used to mimic the detection of subsurface objects. Therefore, there are totally two layers. The top layer is

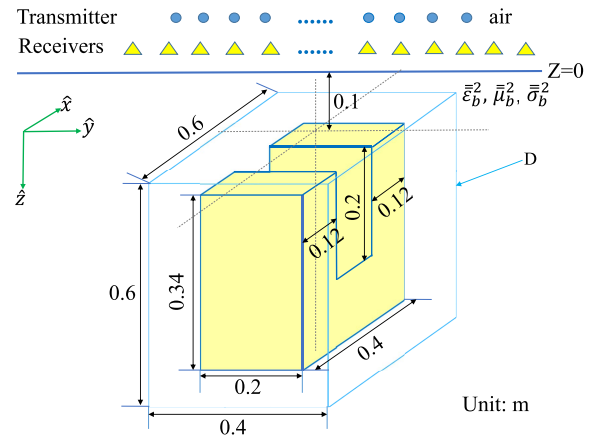


Fig. 5. Configuration of the inversion model with a concave scatterer with the dimensions of 0.4 m \times 0.2 m \times 0.34 m.

air and the bottom layer has the uniaxial dielectric parameters. The transmitters and receivers are placed in the top layer and the arbitrary anisotropic objects are embedded in the bottom layer. In the third model, transmitters and receivers are placed in two sides of the scatterers which are embedded in the middle layer. In all these three cases, 18 unknown parameters are reconstructed simultaneously. The scatterers are embedded in the second layer which has the dielectric parameters as

$$\bar{\varepsilon}_b^2 = \text{diag}\{1.5, 1.5, 2.0\} \quad (27a)$$

$$\bar{\mu}_b^2 = \text{diag}\{1.2, 1.2, 1.8\} \quad (27b)$$

$$\bar{\sigma}_b = \text{diag}\{3, 3, 4\} \text{ mS/m.} \quad (27c)$$

TABLE II
SCATTERER DIELECTRIC PARAMETERS OF THE CONCAVE OBJECT

Parameter	ε_{11}	ε_{12}	ε_{13}	ε_{22}	ε_{23}	ε_{33}	μ_{11}	μ_{12}	μ_{13}	μ_{22}	μ_{23}	μ_{33}	σ_{11}	σ_{12}	σ_{13}	σ_{22}	σ_{23}	σ_{33}
scatterer concave object	2.4	0.6	0.4	2.0	0.5	2.8	1.7	0.5	0.4	1.6	0.5	2.5	5	4	3	6	4	7

Remark: the unit of σ is mS/m.

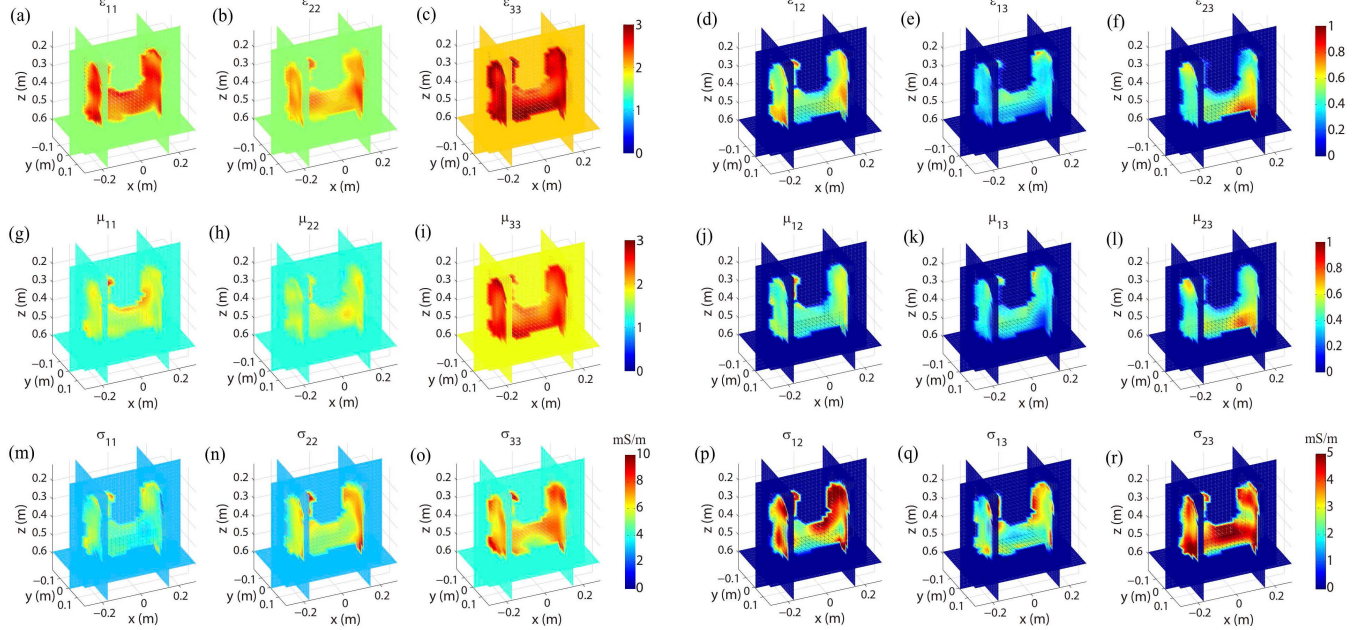


Fig. 6. Reconstructed 3-D profiles of the concave object by VBIM-SCC-SCS. (a)–(l) Relative permittivity. (m)–(r) Conductivity.

All three numerical cases are run on a workstation with 20-cores Xeon E2650 v3 2.3G CPU, 512GB RAM.

A. Concave Object Embedded in the Bottom Layer

As shown in Fig. 5, the concave shape is formed by cutting a small cube with the size of $0.16 \text{ m} \times 0.2 \text{ m} \times 0.2 \text{ m}$ out of a rectangular shape with the dimensions of $0.4 \text{ m} \times 0.2 \text{ m} \times 0.34 \text{ m}$. The centers of the cube and the rectangular shape are $(0, 0, 0.3) \text{ m}$ and $(0, 0, 0.37) \text{ m}$, respectively. The dielectric parameters of the scatterer are listed in Table II.

The reconstructed region D enclosing the object has the dimensions of $0.6 \text{ m} \times 0.4 \text{ m} \times 0.6 \text{ m}$ and is divided into 18 thousand cells. Its center is located at the $(0, 0, 0.4) \text{ m}$. The size of each cell is $\Delta x = \Delta y = \Delta z = 0.02 \text{ m}$. So there are totally 324 thousand unknowns to be reconstructed. A total of 54 transmitters are uniformly located in a $1.6 \text{ m} \times 1 \text{ m}$ plane at $z = -0.2 \text{ m}$. Two operating frequencies, 250 and 300 MHz are adopted. The scattered fields are collected by an array with 96 receivers which are uniformly located in a $3.3 \text{ m} \times 2.1 \text{ m}$ plane at $z = -0.1 \text{ m}$. Thus, there are 124 416 data equations.

We perform the inversion by VBIM-SCC with and without SCS. The VBIM-SCC terminates after 93 iterations when the relative residual error (RRE) of the reconstructed scattered field compared with the measured data is less than the threshold 6×10^{-4} while VBIM-SCC-SCS terminates after 96 iterations. The restructured 3-D profiles and 2-D

slices of the anisotropic dielectric parameters of the concave object by VBIM-SCC-SCS are shown in Figs. 6 and 7, respectively. Note the 2-D slices are displayed with different cross sections for different parameters. The true location and shape of the object are illustrated by dotted boxes. We can see that both the shape and 18 dielectric parameters of the anisotropic concave scatterer are well reconstructed. Fig. 9 shows the reconstructed relative permittivity slices by VBIM-SCC without SCS. By comparing with the permittivity slices shown in Fig. 7, we find VBIM-SCC-SCS outperforms VBIM-SCC since the isolated “scatterer” cells are not completely excluded by VBIM-SCC. Comparisons of other anisotropic parameters show the same results and are not presented. In order to quantitatively evaluate the improvement facilitated by the SCS algorithm, we define the model misfit and data misfit as

$$Err_{model} = \frac{\|\mathbf{md}_R - \mathbf{md}_T\|}{\|\mathbf{md}_T\|} \quad (28a)$$

$$Err_{data} = \frac{\|\mathbf{da}_R - \mathbf{da}_T\|}{\|\mathbf{da}_T\|} \quad (28b)$$

where \mathbf{md}_T is the true model parameter and \mathbf{md}_R is the reconstructed parameter. \mathbf{da}_T is the measured scattered field and \mathbf{da}_R is the reconstructed scattered field when iterations stop. The data misfits of scattered electric and magnetic fields and model misfits of all reconstructed parameters are listed in Table III. We can see that the model misfits of

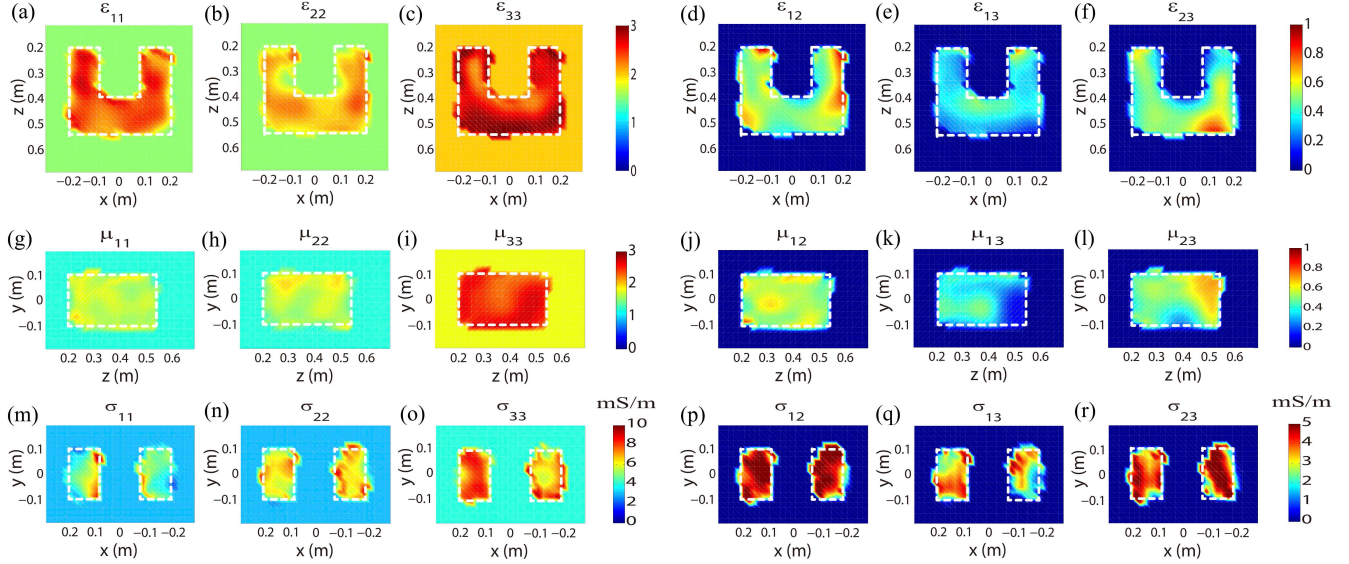


Fig. 7. Detailed 2-D slices of reconstructed results for the concave object by VBIM-SCC-SCS. (a)–(f) xz slices at $y = 0$ m for reconstructed relative permittivity. (g)–(l) yz slices at $x = 0.14$ m for reconstructed relative permeability. (m)–(r) xy slices at $z = 0.26$ m for reconstructed conductivity.

TABLE III
MISFITS FOR VBIM-SCC WITH AND WITHOUT SCS FOR THE CONCAVE SCATTERER

VBIM type \ Misfit	Data misfit(%)												Model misfit(%)											
	Parameter	Electric field	Magnetic field	ϵ_{11}	ϵ_{22}	ϵ_{33}	ϵ_{12}	ϵ_{13}	ϵ_{23}	μ_{11}	μ_{22}	μ_{33}	μ_{12}	μ_{13}	μ_{23}	σ_{11}	σ_{22}	σ_{33}	σ_{12}	σ_{13}	σ_{23}			
VBIM-SCC		0.058	0.058	9.74	6.87	8.34	51.0	53.8	52.7	8.10	7.42	8.34	50.9	54.4	51.1	15.4	16.8	13.8	53.0	53.3	49.2			
VBIM-SCC-SCS		0.049	0.050	9.57	7.18	7.97	48.9	50.2	48.4	8.63	7.58	7.79	48.1	48.2	48.2	16.3	18.0	13.6	53.9	51.8	50.9			

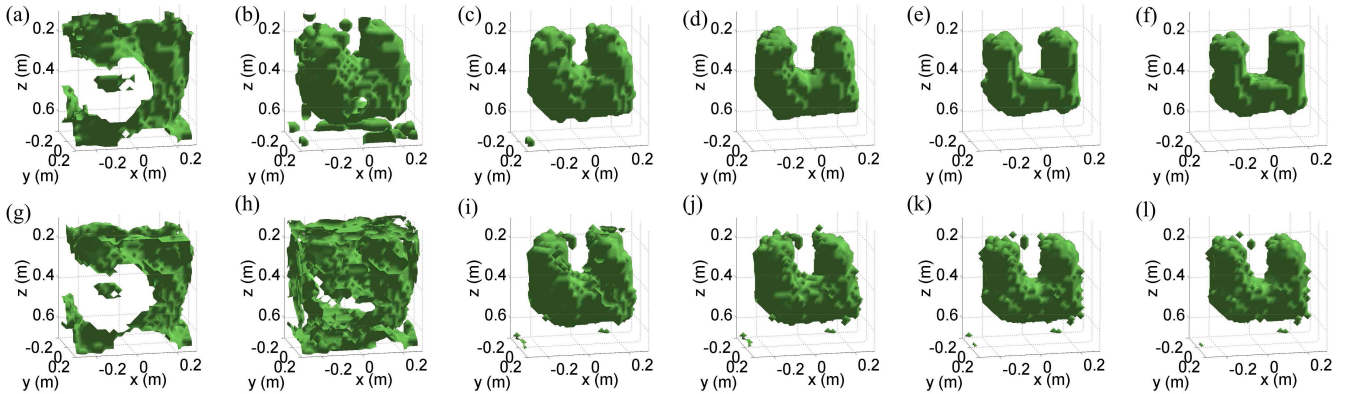


Fig. 8. Structure focusing processes by VBIM-SCC with and without SCS are shown from left to right. (a)–(f) With SCS. (g)–(l) Without SCS. The structure snapshots are taken in the 3rd, 8th, 15th, 22nd, 50th, and the last step in the VBIM iterations.

off-diagonal dielectric parameters are nearly four or five times larger than those of the diagonal ones. The key reason is that the background medium is uniaxial anisotropic, and its off-diagonal dielectric parameters are zero. This makes the denominator of (28a) rather small when the model misfits of off-diagonal parameters are evaluated. In addition, the SCS algorithm not only decreases the data misfits but also reduces the model misfits of most off-diagonal parameters. Although the reductions are not significant, they are obvious. The model misfits of the diagonal dielectric parameters are already small

enough and thus not obviously reduced by the SCS algorithm. The total computation time for VBIM-SCC and VBIM-SCC-SCS are 8.5 and 8.8 h, respectively. Because the SCC keeps reducing the number of unknowns in the iterations, the memory consumption gradually decreases. Maximum memory consumption and minimal memory consumption by VBIM-SCC and VBIM-SCC-SCS are almost the same. They are 150 and 27 GB, respectively.

We can see that the SCS almost has a negligible additional computation cost. Its major contribution is to make the

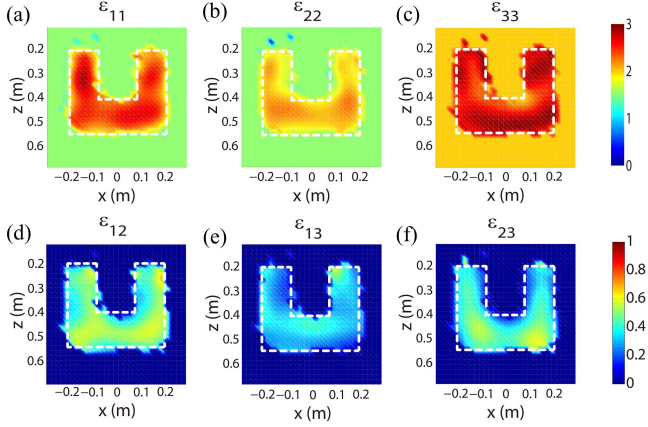


Fig. 9. Reconstructed relative permittivity xz slices at $y = 0$ m by VBIM-SCC without SCS.

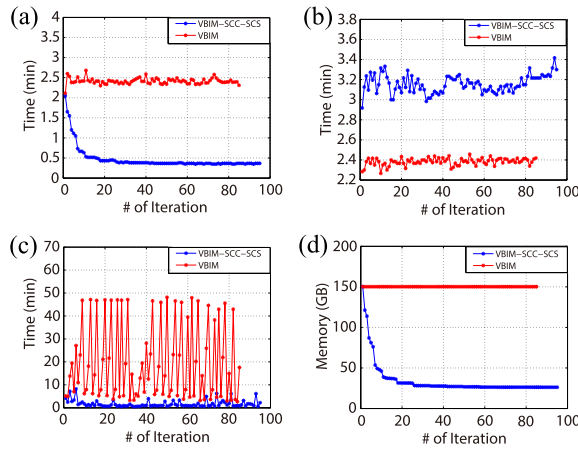


Fig. 10. Computational time and memory consumption of the traditional VBIM algorithm and the VBIM-SCC-SCS algorithm in each iteration step. (a) Time for assembling matrix \mathbf{B}_n in (22) before inversion. (b) Time of BCGS-FFT in the forward computation. (c) Time of CG iteration in the inversion. (d) Total memory consumption.

reconstructed structures smoother. Fig. 8 shows the focusing processes of the scatterer structures acquired by SCC with and without SCS. Each snapshot represents the reconstructed structure in a certain step of VBIM-SCC iterations. We can see that the reconstructed structure gradually focuses on the shape and location of the object. The SCS helps to exclude the isolated faked “scatterer” cells and make the structure smoother.

We also reconstruct the concave scatterer using the traditional VBIM without SCC-SCS and compare its performance with the VBIM-SCC-SCS algorithm. Fig. 10 shows the comparisons for time and memory consumption in each iteration step. The time consumption mainly consists of three parts, BCGS-FFT, assembling matrix \mathbf{B}_n in (22) and the CG iteration. There are three points worth noting in the following.

- 1) Compared with the traditional VBIM which almost takes the same time to assemble the matrix in each iteration, the time for assembling matrix by VBIM-SCC-SCS decreases quickly in first 20 iteration steps and then remains almost unchanged. When the BCGS-FFT-VBIM iterations are executed, the SCC removes

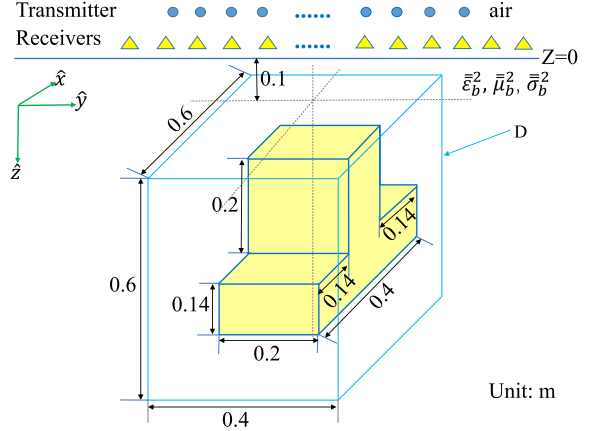


Fig. 11. Configuration of the inversion model with a convex scatterer with the dimensions of $0.4\text{ m} \times 0.2\text{ m} \times 0.34\text{ m}$.

the “background” cells quickly at the beginning and then only removes a small number of “background” cells in the following each iteration step. Therefore, both the time and memory used for assembling matrix decrease quickly at the beginning but almost keep unchanged in following iteration steps, as are shown in Fig. 10(a) and (d), respectively.

- 2) The time consumed by BCGS-FFT almost keeps unchanged for both VBIM and VBIM-SCC-SCS in the iterations. This is because the SCC only changes the matrix used in the inversion. In the forward computation, the domain size remains unchanged even when the SCC is adopted. However, it should be noted that the BCGS solver needs more time in each iteration step when SCC is applied. The SCC-SCS mandatorily modifies the model parameter distribution in the inversion domain solved by the CG solver. As a result, the BCGS-FFT solver requires more iterations to reach the prescribed convergence threshold.
- 3) The CG solver needs less time when SCC-SCS is applied, as is shown in Fig. 10(c). The SCC removes the “background” cells and thus reduces the number of unknowns. The best model parameter distribution becomes easier to find and thus the CG iteration converges faster when SCC is applied. The oscillation trend in Fig. 10(c) for VBIM without SCC-SCS is due to the unstable model parameter distribution acquired in each iteration which is usually caused by complicated anisotropic scatterers.

B. Convex Object Embedded in the Bottom Layer

In this case, we verify the anti-noise ability of the inversion algorithm. The concave object is replaced by a convex object, and the configuration of the inversion model is shown in Fig. 11. The setups of transmitters, receivers, scatterer dielectric parameters, and the inversion domain are the same as those of the last case. White Gaussian noise is added to the simulated scattered field to form synthetic data. We set the power signal-to-noise ratio (SNR) of the synthetic data

TABLE IV
MISFITS FOR VBIM-SCC-SCS WITH DIFFERENT LEVELS OF NOISE CONTAMINATION FOR THE CONVEX SCATTERER

SNR	Misfit		Data misfit(%)												Model misfit(%)											
	Parameter		Electric field	Magnetic field	ε_{11}	ε_{22}	ε_{33}	ε_{12}	ε_{13}	ε_{23}	μ_{11}	μ_{22}	μ_{33}	μ_{12}	μ_{13}	μ_{23}	σ_{11}	σ_{22}	σ_{33}	σ_{12}	σ_{13}	σ_{23}				
Noise-free	0.052		0.053		8.26	5.49	6.67	48.1	57.4	50.7	7.33	6.31	6.81	47.6	53.3	48.9	16.4	16.6	12.2	51.2	59.6	48.6				
30 dB			3.17		3.18	9.51	6.83	8.04	53.4	63.3	58.2	8.50	7.70	7.71	51.9	51.7	54.0	18.4	21.1	13.9	66.5	77.5	62.2			
20 dB			10.05		10.04	10.8	7.76	8.22	59.2	63.9	57.9	8.61	7.98	8.21	59.6	63.5	58.3	25.9	21.0	18.8	60.4	75.3	73.5			

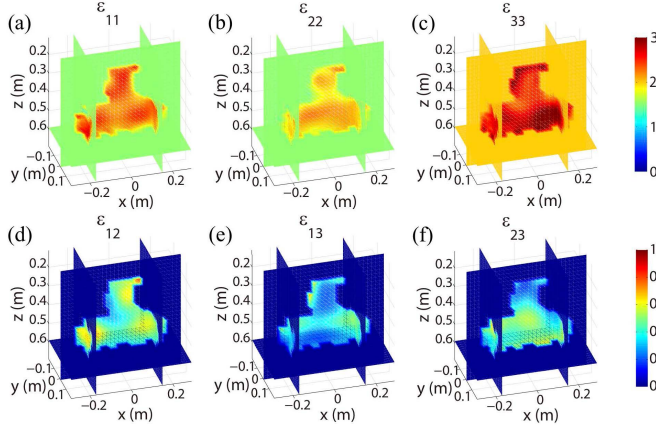


Fig. 12. Reconstructed 3-D profiles of the convex object by VBIM-SCC-SCS.

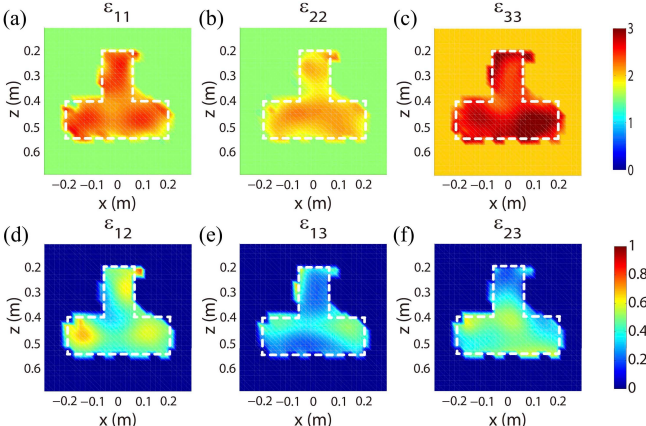


Fig. 13. Detailed xz slices of reconstructed convex object permittivity by VBIM-SCC-SCS when noise-free. The slices are at $y = 0$.

20 and 30 dB, respectively. When VBIM-SCC-SCS inversion procedures terminate, the RRE are 0.052%, 10.05%, and 3.17% for noise-free, SNR = 20 dB, SNR = 30 dB, respectively. The 3-D profiles of the reconstructed results are shown in Fig. 12, and detailed slices for noise-free and SNR = 20 dB are shown in Figs. 13 and 14, respectively. We only show the relative permittivity profiles and the xz slices. Other retrieved parameters and slices are similar and not presented here. The data misfits and model misfits of the reconstruction are listed in Table IV. We can see that the restructured shapes and anisotropic dielectric parameters of the convex scatterer are still reliable even with 20 dB noise contamination. The field misfits are a little larger than the noise to

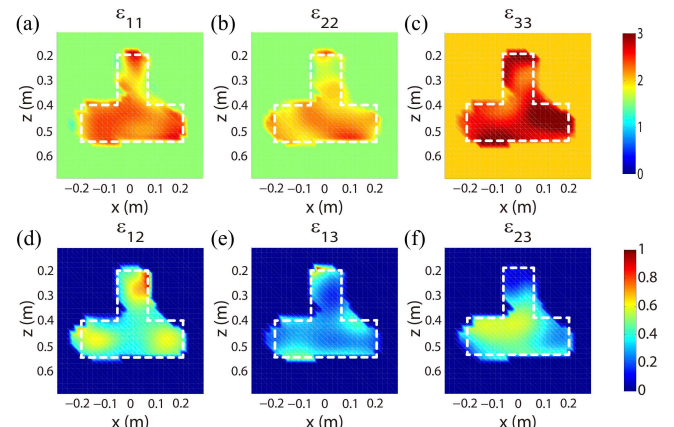


Fig. 14. Detailed xz slices of reconstructed the convex object permittivity by VBIM-SCC-SCS when $SNR = 20$ dB. The slices are at $y = 0$.

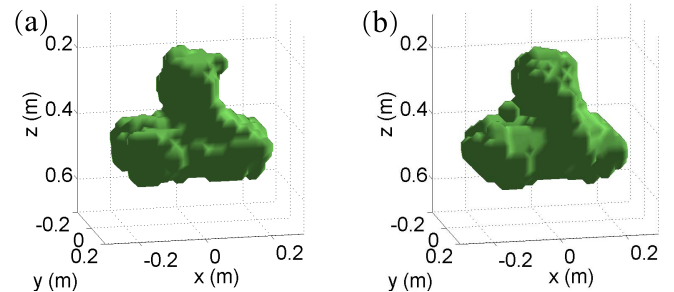


Fig. 15. 3-D iso-surface plots of the reconstructed shapes of the convex object. (a) Noise-free. (b) $SNR = 20$ dB.

signal amplitude ratio, which implies that the VBIM-SCC-SCS has a certain anti-noise ability to retrieve arbitrary anisotropic objects. Fig. 15 shows the 3-D iso-surfaces of the reconstructed convex object when noise free and $SNR = 20$ dB. The noise contamination distorts the reconstructed shape, but the basic convex shape remains discernible. The total time consumption of the inversion for noise free, 20 and 30 dB noise are 7.7, 3.5, and 3.8 h, respectively. The maximum memory consumption for all three cases is 150 GB while the minimal memory consumption is around 20 GB.

C. Two Rectangular Objects Embedded in the Middle Layer

In this case, we apply the VBIM-SCC-SCS algorithm to the reconstruction of multiple anisotropic objects embedded in the middle layer of a three-layer medium. As shown in Fig. 16, the cuboid object has the dimensions of 0.28 m \times 0.2 m \times 0.14 m, and the cube object has the dimensions

TABLE V
SCATTERER DIELECTRIC PARAMETERS OF THE CUBOID AND CUBE

object	Parameter	ε_{11}	ε_{12}	ε_{13}	ε_{22}	ε_{23}	ε_{33}	μ_{11}	μ_{12}	μ_{13}	μ_{22}	μ_{23}	μ_{33}	σ_{11}	σ_{12}	σ_{13}	σ_{22}	σ_{23}	σ_{33}
cuboid		2.5	0.3	0.3	2.0	0.6	2.8	1.4	0.6	0.3	1.8	0.3	2.2	5	2	3	6	4	7
cube		2.0	0.6	0.3	2.5	0.3	2.4	1.8	0.3	0.3	1.4	0.6	2.6	7	4	3	6	2	5

Remark: the unit of σ is mS/m.

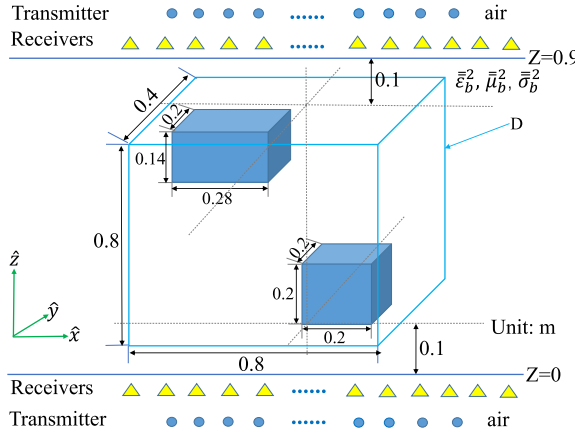


Fig. 16. Configuration of the two-object model with a cuboid scatterer and a cube scatterer with the dimensions of $0.28 \text{ m} \times 0.2 \text{ m} \times 0.14 \text{ m}$ and $0.2 \text{ m} \times 0.2 \text{ m} \times 0.2 \text{ m}$, respectively.

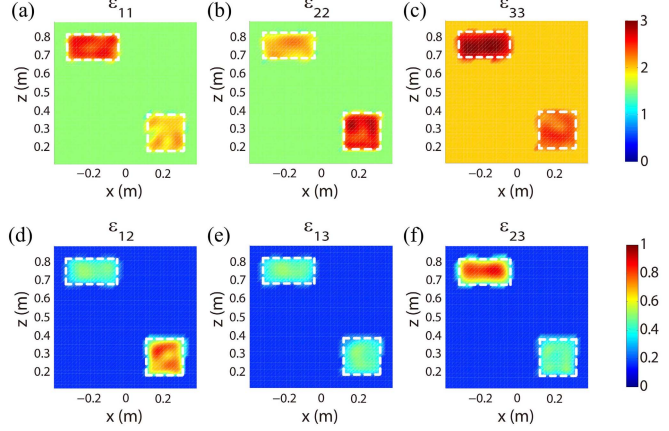


Fig. 18. Detailed slices of reconstructed relative permittivity values for two objects when noise free. The xz slices are at $y = 0$.

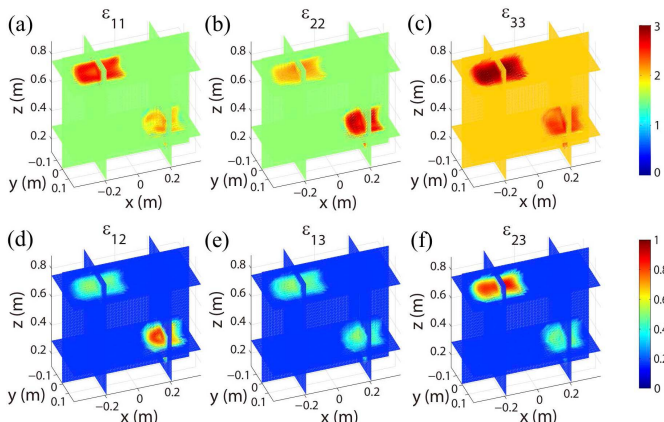


Fig. 17. 3-D reconstructed profiles of the relative permittivity values of two objects by VBIM-SCC-SCS.

of $0.2 \text{ m} \times 0.2 \text{ m} \times 0.2 \text{ m}$. The dielectric parameters of two objects are listed in Table V.

The reconstructed region enclosing two objects has the dimensions of $0.8 \text{ m} \times 0.4 \text{ m} \times 0.8 \text{ m}$ and is divided into 32 thousand cells. Its center is located at $(0, 0, 0.5) \text{ m}$. The size of each cell is $\Delta x = \Delta y = \Delta z = 0.02 \text{ m}$. So there are totally 576 thousand unknowns to be reconstructed. A total of 64 transmitters are uniformly placed in two $1.4 \text{ m} \times 0.6 \text{ m}$ planes at $z = -0.2 \text{ m}$ and $z = 1.2 \text{ m}$, respectively. Three operation frequencies 250, 300 and 350 MHz are chosen. The scattered fields are collected by two arrays with 90 receivers which are uniformly located at $z = -0.1 \text{ m}$

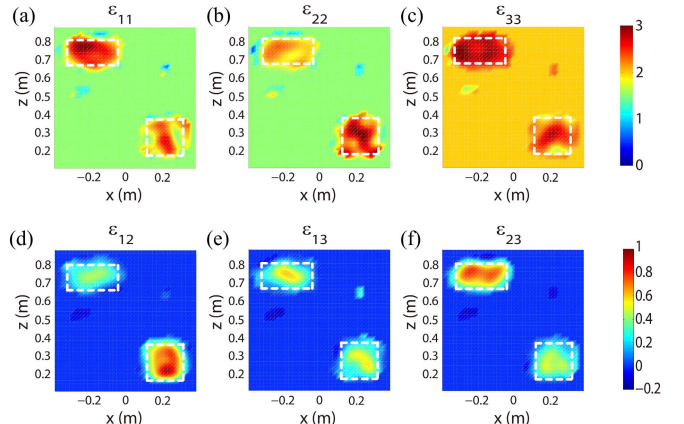


Fig. 19. Detailed slices of reconstructed results of the relative permittivity for two objects when $\text{SNR} = 20 \text{ dB}$. The xz slices are at $y = 0$.

and $z = 1 \text{ m}$ planes, respectively. Thus, there are totally 207360 data equations.

The reconstructed 3-D profiles of the permittivity of two objects are shown in Fig. 17. We can see the rectangular shapes of two objects are almost precisely reconstructed in all three directions. The xz slices at $y = 0$ are given in Fig. 18. Clearly, both the permittivity values and geometry shapes are well reconstructed. Similar as in the last case, we also add a 20 dB Gaussian white noise to the scattered field and perform the VBIM-SCC-SCS inversion. The 2-D xz slices are shown in Fig. 19. Compared with the results shown in Fig. 18, the geometry shapes of two objects are slightly distorted. In addition, some faked isolated small scatterers show up.

TABLE VI

MISFITS FOR VBIM-SCC-SCS WITH DIFFERENT LEVELS OF NOISE CONTAMINATION FOR THE TWO RECTANGULAR SCATTERERS

SNR	Misfit		Data misfit(%)															Model misfit(%)														
	Parameter		Electric field	Magnetic field	ε_{11}	ε_{22}	ε_{33}	ε_{12}	ε_{13}	ε_{23}	μ_{11}	μ_{22}	μ_{33}	μ_{12}	μ_{13}	μ_{23}	σ_{11}	σ_{22}	σ_{33}	σ_{12}	σ_{13}	σ_{23}										
Noise-free	0.072	0.081	3.68	3.93	3.02	32.0	35.1	35.8	3.18	3.46	3.58	35.1	45.1	37.4	9.57	9.60	5.83	39.2	35.4	40.0												
20 dB	10.47	10.58	8.86	9.10	6.01	49.7	62.3	50.3	8.21	7.66	6.78	56.4	68.9	57.9	18.7	20.5	13.9	80.4	75.1	83.8												

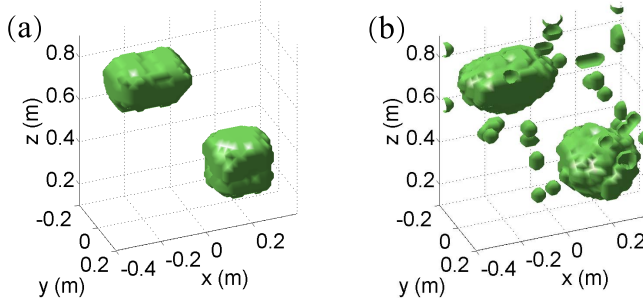


Fig. 20. 3-D iso-surface plots of the reconstructed two objects. (a) Noise-free. (b) SNR = 20 dB.

This is more obviously illustrated by the structure iso-surface plots shown in Fig. 20. One interesting observation is that the reconstructed cube appears spherical when the scattered fields are contaminated by noise. The distorted shape of the reconstructed result is to compensate for the scattered field changes caused by noise. Because the cost function used in VBIM is defined by the L2 norm, the shape tends to be spherical. The data misfits and model misfits of the reconstruction are listed in Table VI. The total time consumption for the noise-free and 20 dB noise cases are 20.8 and 8.3 h, respectively. Maximum memory consumption for both cases is 447 GB while the minimal memory consumption is around 45 GB.

V. CONCLUSION

In this article, the BCGS-FFT fast solver is employed to solve the CFVIE formulated for the EM scattering of magnetodielectric objects with arbitrary anisotropy embedded in a layered uniaxial background medium. Comparisons with FEM computation show that both the total fields and scattered fields solved by BCGS-FFT are precise and reliable.

In the inversion, 18 dielectric parameters per cell of the arbitrary anisotropic scatterers are reconstructed simultaneously by VBIM-SCC, which gradually focuses the scatterer geometry to its true shapes and locations in each VBIM iteration step. The SCS algorithm proposed in this article helps to make the reconstructed shapes smoother by excluding the faked “scatterer” blocks attached to the true scatterer surfaces or embedded in the background medium. Anti-noise tests show that the basic shapes of the reconstruction by VBIM-SCC-SCS are discernible when 20 dB Gaussian white noise is added. The dielectric parameter values are also reliable although the model misfits increase. This shows that the VBIM-SCC-SCS algorithm has a certain anti-noise ability.

However, there are three types of EM inverse scattering problems which cannot be solved by the current algorithm.

First, the inversion of isotropic scatterers cannot be accomplished by VBIM-SCC-SCS because the SCC is based on Monte Carlo method. The sampling space is too limited to obtain a reliable statistical result for isotropic inverse scattering. Second, scatterers with more complicated geometry structures cannot be reconstructed by VBIM-SCC-SCS. For example, a cuboid object is formed by connecting the concave and convex objects used in this article. Since the SCC is used to distinguish the “scatterer” cell and “background” cell, it is incapable of depicting the jagged geometry boundary between the concave and convex scatterers. As a result, the reconstructed dielectric parameters of the concave and convex objects will deviate away from the true values due to the ill posedness of the inversion. Third, VBIM-SCC-SCS cannot deal with low SNR EM scattering problems. In this article, we use the 20 and 30 dB noise contamination. We made a trial and decreased the SNR to 10 dB. The VBIM cannot converge correctly. The key reason is that the VBIM-SCC is a deterministic algorithm. When the noise is very large, it is too difficult for the iterative solver to find a stable solution to minimize the cost function. All these three issues will be investigated in our future work by a sophisticated combination of the EM inverse scattering solver and a machine learning technique.

In addition, the inversion results presented in this article are only for numerical simulations. The reconstruction of arbitrary anisotropic scatterers embedded in layered uniaxial media from laboratory-measured scattered data will be rather challenging. First, the EM wave scattering by measurement instruments or laboratory surroundings can cause errors in the measured scattered data. In previous work, the measurement of EM scattering from isotropic objects embedded in layered media was conducted in a rectangular tub containing a lossy fluid to reduce the reflections from the surrounding environment [3]. However, due to the energy attenuation, the measured signals were weak and SNR was lowered. There were also successful measurements of scattered EM fields in air. They were actually performed in an anechoic chamber [53]. These experiments were only for a homogeneous background media instead of a layered medium. Second, the antennas used in [3] have the unique vertical polarization. Such a configuration works for the inversion of isotropic scatterers. However, it is problematic for the inversion of anisotropic scatterers since some components of the dielectric parameter tensors are not sensitive to the change of vertical electric fields. Therefore, in order to perform the inversion for laboratory measurements, the polarization of both the transmitting and receiving antennas should be properly configured to guarantee the effective measurements of all six components of electric

and magnetic fields. Third, it is not easy to construct both the uniaxial background media and the arbitrary anisotropic scatterer. One possible solution is to use thin isotropic slabs stacked periodically to mimic the uniaxial background media. Then, we can use the uniaxial crystal but rotate its optical axial to simulate the arbitrary anisotropic scatterer with symmetrical dielectric parameter tensors. However, such an experiment is too challenging in the current stage and will be left as our future research work.

REFERENCES

- [1] Q. H. Liu *et al.*, "Active microwave imaging. I. 2-D forward and inverse scattering methods," *IEEE Trans. Microw. Theory Tech.*, vol. 50, no. 1, pp. 123–133, Jan. 2002.
- [2] C. Yu *et al.*, "Active microwave imaging II: 3-D system prototype and image reconstruction from experimental data," *IEEE Trans. Microw. Theory Techn.*, vol. 56, no. 4, pp. 991–1000, Apr. 2008.
- [3] C. Yu *et al.*, "Microwave imaging in layered media: 3-D image reconstruction from experimental data," *IEEE Trans. Antennas Propag.*, vol. 58, no. 2, pp. 440–448, Feb. 2010.
- [4] Y. Chu *et al.*, "Fast microwave through wall imaging method with inhomogeneous background based on Levenberg–Marquardt algorithm," *IEEE Trans. Microw. Theory Tech.*, vol. 67, no. 3, pp. 1138–1147, Mar. 2019.
- [5] T. Lan, H. Liu, N. Liu, J. Li, F. Han, and Q. H. Liu, "Joint inversion of electromagnetic and seismic data based on structural constraints using variational born iteration method," *IEEE Trans. Geosci. Remote Sens.*, vol. 56, no. 1, pp. 436–445, Jan. 2018.
- [6] T. Lan, N. Liu, F. Han, and Q. H. Liu, "Joint petrophysical and structural inversion of electromagnetic and seismic data based on volume integral equation method," *IEEE Trans. Geosci. Remote Sens.*, vol. 57, no. 4, pp. 2075–2086, Apr. 2019.
- [7] L. Gürel and M. I. Aksun, "Electromagnetic scattering solution of conducting strips in layered media using the fast multipole method," *IEEE Microw. Guided Wave Lett.*, vol. 6, no. 8, pp. 277–279, Aug. 1996.
- [8] F. Han, J. L. Zhuo, N. Liu, Y. Liu, H. Liu, and Q. H. Liu, "Fast solution of electromagnetic scattering for 3-D inhomogeneous anisotropic objects embedded in layered uniaxial media by the BCGS-FFT method," *IEEE Trans. Antennas Propag.*, vol. 67, no. 3, pp. 1748–1759, Mar. 2019.
- [9] Y. Hu, Y. Fang, D. Wang, Y. Zhong, and Q. H. Liu, "Electromagnetic waves in multilayered generalized anisotropic media," *IEEE Trans. Geosci. Remote Sens.*, vol. 56, no. 10, pp. 5758–5766, Oct. 2018.
- [10] G. P. Zouros and G. C. Kokkorakis, "Electromagnetic scattering by a general rotationally symmetric inhomogeneous anisotropic sphere," *IEEE Trans. Microw. Theory Techn.*, vol. 63, no. 10, pp. 3054–3065, Oct. 2015.
- [11] D. Pardo, M. J. Nam, C. Torres-Verdín, M. G. Hoversten, and I. Garay, "Simulation of marine controlled source electromagnetic measurements using a parallel Fourier hp -finite element method," *Comput. Geosci.*, vol. 15, pp. 53–67, Jan. 2011.
- [12] Y. Zhong, M. Lambert, D. Lesselier, and X. Chen, "Electromagnetic response of anisotropic laminates to distributed sources," *IEEE Trans. Antennas Propag.*, vol. 62, no. 1, pp. 247–256, Jan. 2014.
- [13] J. Zhuo, L. Ye, F. Han, L. Xiong, and Q. H. Liu, "Multiparametric electromagnetic inversion of 3-D biaxial anisotropic objects embedded in layered uniaxial media using VBIM enhanced by structural consistency constraint," *IEEE Trans. Antennas Propag.*, to be published.
- [14] F.-G. Hu, C.-F. Wang, and Y.-B. Gan, "Efficient calculation of electromagnetic scattering from cavities coated with bianisotropic media using FE-BI method with higher-order tetrahedral elements," in *Proc. IEEE Antennas Propag. Soc. Int. Symp.*, Singapore, Jul. 2006, pp. 3883–3886.
- [15] X. Millard and Q. H. Liu, "A fast volume integral equation solver for electromagnetic scattering from large inhomogeneous objects in planarly layered media," *IEEE Trans. Antennas Propag.*, vol. 51, no. 9, pp. 2393–2401, Sep. 2003.
- [16] L. E. Sun, "Electromagnetic modeling of inhomogeneous and anisotropic structures by volume integral equation methods," *Waves Random Complex Media*, vol. 25, no. 4, pp. 536–548, 2015.
- [17] G. P. Zouros and G. C. Kokkorakis, "Electromagnetic scattering by an inhomogeneous gyroelectric sphere using volume integral equation and orthogonal Dini-type basis functions," *IEEE Trans. Antennas Propag.*, vol. 63, no. 6, pp. 2665–2676, Jun. 2015.
- [18] S. M. Rao, D. R. Wilton, and A. W. Glisson, "Electromagnetic scattering by surfaces of arbitrary shape," *IEEE Trans. Antennas Propagat.*, vol. AP-30, no. 3, pp. 409–418, May 1982.
- [19] M. S. Tong, Y. Q. Zhang, R. P. Chen, and C. X. Yang, "Fast solutions of volume integral equations for electromagnetic scattering by large highly anisotropic objects," *IEEE Trans. Microw. Theory Tech.*, vol. 62, no. 7, pp. 1429–1436, Jul. 2014.
- [20] K. A. Michalski and D. Zheng, "Electromagnetic scattering and radiation by surfaces of arbitrary shape in layered media, Part I: Theory," *IEEE Trans. Antennas Propag.*, vol. 38, no. 3, pp. 335–344, Mar. 1990.
- [21] K. A. Michalski and D. Zheng, "Electromagnetic scattering and radiation by surfaces of arbitrary shape in layered media, Part II: Implementation and results for contiguous half-spaces," *IEEE Trans. Antennas Propag.*, vol. 38, no. 3, pp. 345–352, Mar. 1990.
- [22] M. Maddah-Ali, S. H. H. Sadeghi, and M. Dehmollaian, "A method of moments for analysis of electromagnetic scattering from inhomogeneous anisotropic bodies of revolution," *IEEE Trans. Antennas Propag.*, vol. 66, no. 6, pp. 2976–2986, Jun. 2018.
- [23] Z. Zhang *et al.*, "Higher order VIE method based on non-conformal discretisation for EM scattering from anisotropic objects," *IET Microw. Antennas Propag.*, vol. 13, no. 9, pp. 1338–1344, Jul. 2019.
- [24] X. M. Xu and Q. H. Liu, "The BCGS-FFT method for electromagnetic scattering from inhomogeneous objects in a planarly layered medium," *IEEE Antennas Wireless Propag. Lett.*, vol. 1, no. 1, pp. 77–80, 2002.
- [25] D. V. Ginstre, H. Rogier, F. Olyslager, and D. De Zutter, "A fast multipole method for layered media based on the application of perfectly matched layers—The 2-D case," *IEEE Trans. Antennas Propag.*, vol. 52, no. 10, pp. 2631–2640, Oct. 2004.
- [26] B. E. Barrowes, C. O. Ao, F. L. Teixeira, and J. A. Kong, "Sparse matrix/canonical grid method applied to 3-D dense medium simulations," *IEEE Trans. Antennas Propag.*, vol. 51, no. 1, pp. 48–58, Jan. 2003.
- [27] L. Hu, L.-W. Li, and T.-S. Yeo, "Analysis of scattering by large inhomogeneous BI-anisotropic objects using AIM," *Progr. Electromagn. Res.*, vol. 99, pp. 21–36, 2009.
- [28] X.-C. Nie, L.-W. Li, N. Yuan, T. S. Yeo, and Y.-B. Gan, "Precorrected-FFT solution of the volume Integral equation for 3-D inhomogeneous dielectric objects," *IEEE Trans. Antennas Propag.*, vol. 53, no. 1, pp. 313–320, Jan. 2005.
- [29] R. W. Deming and A. J. Devaney, "Diffraction tomography for multi-monostatic ground penetrating radar imaging," *Inverse Problems*, vol. 13, no. 1, pp. 29–45, 1997.
- [30] L. Poli, G. Oliveri, and A. Massa, "Microwave imaging within the first-order Born approximation by means of the contrast-field Bayesian compressive sensing," *IEEE Trans. Antennas Propag.*, vol. 60, no. 6, pp. 2865–2879, Jun. 2012.
- [31] P. A. Barrière, J. Idier, Y. Goussard, and J.-J. Laurin, "Fast solutions of the 2D inverse scattering problem based on a TSVD approximation of the internal field for the forward model," *IEEE Trans. Antennas Propag.*, vol. 58, no. 12, pp. 4015–4024, Dec. 2010.
- [32] W. C. Chew and Y. M. Wang, "Reconstruction of two-dimensional permittivity distribution using the distorted Born iterative method," *IEEE Trans. Med. Imag.*, vol. 9, no. 2, pp. 218–225, Jun. 1990.
- [33] A. Abubakar, P. M. van den Berg, and J. J. Mallorqui, "Imaging of biomedical data using a multiplicative regularized contrast source inversion method," *IEEE Trans. Microw. Theory Techn.*, vol. 50, no. 7, pp. 1761–1771, Jul. 2002.
- [34] Y. Hu, Y. Fang, D. LaBrecque, M. Ahmadian, and Q. H. Liu, "Reconstruction of high-contrast proppant in hydraulic fractures with galvanic measurements," *IEEE Trans. Geosci. Remote Sens.*, vol. 56, no. 4, pp. 2066–2073, Apr. 2018.
- [35] C. Yu, M. Yuan, and Q. H. Liu, "Reconstruction of 3D objects from multi-frequency experimental data with a fast DBIM-BCGS method," *Inverse Problems*, vol. 25, no. 2, 2009, Art. no. 024007.
- [36] X. Ye and X. Chen, "Subspace-based distorted-born iterative method for solving inverse scattering problems," *IEEE Trans. Antennas Propag.*, vol. 65, no. 12, pp. 7224–7232, Dec. 2017.
- [37] N. Zaiping, Y. Feng, Z. Yanwen, and Z. Yerong, "Variational Born iteration method and its applications to hybrid inversion," *IEEE Trans. Geosci. Remote Sens.*, vol. 38, no. 4, pp. 1709–1715, Jul. 2000.
- [38] P.-A. Barrière, J. Idier, J.-J. Laurin, and Y. Goussard, "Contrast source inversion method applied to relatively high contrast objects," *Inverse Problems*, vol. 27, no. 7, Jul. 2011, Art. no. 075012.
- [39] X. Chen, "Subspace-based optimization method for solving inverse-scattering problems," *IEEE Trans. Geosci. Remote Sens.*, vol. 48, no. 1, pp. 42–49, Jan. 2009.

- [40] L. Pan, Y. Zhong, X. Chen, and S. P. Yeo, "Subspace-based optimization method for inverse scattering problems utilizing phaseless data," *IEEE Trans. Geosci. Remote Sens.*, vol. 49, no. 3, pp. 981–987, Mar. 2011.
- [41] K. Agarwal, L. Pan, and X. Chen, "Subspace-based optimization method for reconstruction of 2-D complex anisotropic dielectric objects," *IEEE Trans. Microw. Theory Techn.*, vol. 58, no. 4, pp. 1065–1074, Mar. 2010.
- [42] X. Chen, "Subspace-based optimization method for inverse scattering problems with an inhomogeneous background medium," *Inverse Problems*, vol. 26, no. 7, May 2010, Art. no. 074007.
- [43] K. Xu, Y. Zhong, X. Chen, and D. Lesselier, "A fast integral equation-based method for solving electromagnetic inverse scattering problems with inhomogeneous background," *IEEE Trans. Antennas Propag.*, vol. 66, no. 8, pp. 4228–4239, Aug. 2018.
- [44] K. Yang and A. E. Yilmaz, "FFT-accelerated analysis of scattering from complex dielectrics embedded in uniaxial layered media," *IEEE Trans. Geosci. Remote Sens.*, vol. 10, no. 4, pp. 662–666, Jul. 2013.
- [45] G. D. Kolezas and G. P. Zouros, "CFVIE formulation for EM scattering on inhomogeneous anisotropic—Metallic objects," *IEEE Trans. Antennas Propag.*, vol. 65, no. 7, pp. 3788–3793, Jul. 2017.
- [46] T. P. Harrigan and R. W. Mann, "Characterization of microstructural anisotropy in orthotropic materials using a second rank tensor," *J. Mater. Sci.*, vol. 19, no. 3, pp. 761–767, 1984.
- [47] C. A. Balanis, *Advanced Engineering Electromagnetics*. New York, NY, USA: Wiley, 2012, ch. 7.
- [48] K. A. Michalski and J. R. Mosig, "Multilayered media Green's functions in integral equation formulations," *IEEE Trans. Antennas Propag.*, vol. 45, no. 3, pp. 508–519, Mar. 1997.
- [49] P. Zwamborn and P. M. van den Berg, "The three dimensional weak form of the conjugate gradient FFT method for solving scattering problems," *IEEE Trans. Microw. Theory Tech.*, vol. 40, no. 9, pp. 1757–1766, Sep. 1992.
- [50] C. L. Lawson and R. J. Hanson, Eds., *Solving Least Squares Problems*. Englewood Cliffs, NJ, USA: Prentice-Hall, 1974.
- [51] M. F. Catedra, R. P. Torres, J. Basterrechea, and E. Gago, Eds., *The CG-FFT Method: Application of Signal Processing Techniques to Electromagnetics*. Boston, MA, USA: Artech House, 1994.
- [52] M. Commer and G. A. Newman, "New advances in three-dimensional controlled-source electromagnetic inversion," *Geophys. J. Int.*, vol. 172, no. 2, pp. 513–535, Feb. 2008.
- [53] J.-M. Geffrin, P. Sabouroux, and C. Eyraud, "Free space experimental scattering database continuation: Experimental set-up and measurement precision," *Inverse Problems*, vol. 21, no. 6, p. S117, 2005.



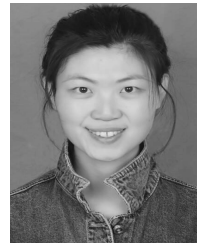
Jiawen Li received the B.S. degree and the M.S. degree in electronic science and technology from the Wuhan University of Technology, Wuhan, China, in 2011 and 2016, respectively. He is currently pursuing the Ph.D. degree with Xiamen University, Xiamen, China.

His current research interests include electromagnetic scattering and inverse scattering in complex media and the full-wave inversion of anisotropic targets.



Jianliang Zhuo received the B.S. degree in communication engineering and business administration and the M.S. degree in communication and information system from the University of Electronic Science and Technology of China, Chengdu, China, in 2007 and 2011, respectively, and the Ph.D. degree in physical electronics from Xiamen University, Xiamen, China, in 2018.

His current research interests include fast forward solvers in electromagnetics and inverse scattering methods for microelectronics and RF systems.



Zhen Guan received the B.S. degree in mathematics and applied mathematics and the M.S. degree in fundamental mathematics from the Tianjin University of Technology and Education, Tianjin, China, in 2014 and 2017, respectively. She is currently pursuing the Ph.D. degree in computational science with Xiamen University, Xiamen, China.

Her current research interests include the fast algorithms for computational electromagnetics and electromagnetic scattering and inverse scattering problems.



Feng Han (M'17) received the B.S. degree in electronic science from Beijing Normal University, Beijing, China, in 2003, the M.S. degree in geophysics from Peking University, Beijing, in 2006, and the Ph.D. degree in electrical engineering from Duke University, Durham, NC, USA, in 2011.

He is currently an Assistant Professor with the Institute of Electromagnetics and Acoustics, Xiamen University, Xiamen, China. His current research interests include ionosphere remote sensing by radio atmospherics, electromagnetic full-wave inversion by integral equations, reverse time migration image, and the design of an electromagnetic detection system.



Qing Huo Liu (S'88–M'89–SM'94–F'05) received the B.S. and M.S. degrees in physics from Xiamen University, Xiamen, China, in 1983 and 1986, respectively, and the Ph.D. degree in electrical engineering from the University of Illinois at Urbana-Champaign, Champaign, IL, USA, in 1989.

He was with the Electromagnetics Laboratory, University of Illinois at Urbana-Champaign, as a Research Assistant, from September 1986 to December 1988, and a Post-Doctoral Research Associate, from January 1989 to February 1990. He was a Research Scientist and the Program Leader with Schlumberger-Doll Research, Ridgefield, CT, USA, from 1990 to 1995. From 1996 to May 1999, he was an Associate Professor with New Mexico State University, Las Cruces, NM, USA. Since June 1999, he has been with Duke University, Durham, NC, USA, where he is currently a Professor of electrical and computer engineering. He has published over 400 articles in refereed journals and 500 articles in conference proceedings. His current research interests include computational electromagnetics and acoustics, inverse problems, and their application in nanophotonics, geophysics, biomedical imaging, and electronic packaging.

Dr. Liu is a fellow of the Acoustical Society of America, the Electromagnetics Academy, and The Optical Society of America. He serves as the Founding Editor-in-Chief for the IEEE JOURNAL ON MULTISCALE AND MULTIPHYSICS COMPUTATIONAL TECHNIQUES, the Deputy Editor-in-Chief for *Progress in Electromagnetics Research*, an Associate Editor for the IEEE TRANSACTIONS ON GEOSCIENCE AND REMOTE SENSING, and an Editor for the *Journal of Computational Acoustics*.